REGULAR PAPER

ACTA PHYSIOLOGICA

Reliable kidney size determination by magnetic resonance imaging in pathophysiological settings

Thomas Gladytz[1] | **Jason M. Millward[1]** (iD) | **Kathleen Cantow[2]** (iD) | **Luis Hummel[2]** (iD) |
Kaixuan Zhao[1] (iD) | **Bert Flemming[2]** | **João S. Periquito[1,2]** (iD) | **Andreas Pohlmann[1]** (iD) |
Sonia Waiczies[1] (iD) | **Erdmann Seeliger[2]** (iD) | **Thoralf Niendorf[1,3]** (iD)

[1]Berlin Ultrahigh Field Facility (B.U.F.F.), Max Delbrück Center for Molecular Medicine in the Helmholtz Association, Berlin, Germany

[2]Institute of Physiology, Charité-Universitätsmedizin Berlin, Campus Mitte, Berlin, Germany

[3]Experimental and Clinical Research Center, a joint cooperation between the Charité Medical Faculty and the Max Delbrück Center for Molecular Medicine in the Helmholtz Association, Berlin, Germany

Correspondence
Thoralf Niendorf, Max Delbrück Center for Molecular Medicine in the Helmholtz Association, Robert-Rössle-Str. 10 13125 Berlin, Germany.
Email: thoralf.niendorf@mdc-berlin.de

Funding information
Deutsche Forschungsgemeinschaft (DFG, German Research Foundation), Grant/Award Number: 394046635, SFB 1365 and RENOPROTECTION

Abstract

Aim: Kidney diseases constitute a major health challenge, which requires noninvasive imaging to complement conventional approaches to diagnosis and monitoring. Several renal pathologies are associated with changes in kidney size, offering an opportunity for magnetic resonance imaging (MRI) biomarkers of disease. This work uses dynamic MRI and an automated bean-shaped model (ABSM) for longitudinal quantification of pathophysiologically relevant changes in kidney size.

Methods: A geometry-based ABSM was developed for kidney size measurements in rats using parametric MRI (T_2, T_2* mapping). The ABSM approach was applied to longitudinal renal size quantification using occlusion of the (a) suprarenal aorta or (b) the renal vein, (c) increase in renal pelvis and intratubular pressure and (d) injection of an X-ray contrast medium into the thoracic aorta to induce pathophysiologically relevant changes in kidney size.

Results: The ABSM yielded renal size measurements with accuracy and precision equivalent to the manual segmentation, with >70-fold time savings. The automated method could detect a ~7% reduction (aortic occlusion) and a ~5%, a ~2% and a ~6% increase in kidney size (venous occlusion, pelvis and intratubular pressure increase and injection of X-ray contrast medium, respectively). These measurements were not affected by reduced image quality following administration of ferumoxytol.

Conclusion: Dynamic MRI in conjunction with renal segmentation using an ABSM supports longitudinal quantification of changes in kidney size in pathophysiologically relevant experimental setups mimicking realistic clinical scenarios. This can potentially be instrumental for developing MRI-based diagnostic tools for various kidney disorders and for gaining new insight into mechanisms of renal pathophysiology.

KEYWORDS

acute kidney injury, automated bean-shaped model, kidney size, magnetic resonance imaging, pathophysiology of renal disorders, rats, segmentation

ACTA PHYSIOLOGICA

1 | INTRODUCTION

Kidney diseases are a major health issue, with increasing incidence and an estimated five to 10 million deaths per year worldwide.[1-3] Whilst several biomarkers are currently being investigated for diagnosis of renal diseases, to date, clinical point-of-care biomarkers are still lacking for major renal diseases.[4-7] To address this urgent unmet clinical need, noninvasive imaging may provide markers to inform on the different stages of renal pathophysiology, improve prediction and interception of disease progression and evaluate treatment of renal disease.[3,8-18]

An increasing body of literature outlines the potential of noninvasive imaging in evaluating renal size as a clinical parameter in the diagnosis, treatment and determination of prognosis in renal disease. In patients suffering from polycystic kidney disease (PKD) kidney size correlates with disease progression and the decline in glomerular filtration rate.[19-21] Consequently, the US Food and Drug Administration and the European Medicines Agency list renal size as a prognostic biomarker for use in clinical trials of new therapies for autosomal dominant PKD (ADPKD).[22,23] Detecting renal size reduction due to parenchymal atrophy, sclerosis and fibrosis has long been recognized as a tool to identify chronic kidney disease (CKD) and to determine its severity.[24,25] Renal size measured from ultrasound images is currently included as a prognostic imaging biomarker for diabetic kidney disease.[26] A recent position paper from the European Cooperation in Science and Technology Action PARENCHIMA included the longitudinal monitoring of renal size via magnetic resonance imaging (MRI) as a key measure for several kidney disorders including ADPKD, hyperfiltration in early diabetic nephropathy, renal transplants, renal artery stenosis and vesicoureteral reflux.[17]

The fact that changes in renal size are indicative of pathophysiologic developments has been demonstrated in a variety of experimental models. Preclinical models emulating clinical conditions such as acute total or chronic partial ureteral obstructions due to urolithiasis, congenital malformations or during upper urinary tract endourologic procedures indicate that the ensuing congestion increases not just intratubular but also intrarenal pressure.[27-30] As the renal capsule is relatively rigid compared to the rest of the kidney, an increase in intrarenal pressure decreases renal blood flow, thereby diminishing renal oxygen supply.[31] In general, this results in renal tissue hypoxia, a pathophysiologic hallmark of acute kidney injury (AKI) and its potential progression to CKD.[32-38] Administration of X-ray contrast media (CM) for cardiac procedures can induce AKI.[34,39] Animal studies emulating such procedures demonstrated a decrease of up to 60% in cortical and medullary blood perfusion and tissue oxygenation following CM administration. One reason behind this tissue hypoperfusion and hypoxia is the increase in tubular fluid viscosity upon CM application, which results in increased intratubular pressure. The ensuing increase in intrarenal pressure compresses intrarenal vessels.[40-43] The increase in intrarenal pressure results in an increase in kidney size. Also, obstruction of the renal vein, whether short-term (eg, during partial nephrectomy) or slowly developing over a long term (eg, due to renal cell carcinoma-derived thrombus formation), increases renal size whilst at the same time compressing intrarenal vessels, thus leading to tissue hypoxia.[27,44-46] Studies that include or emulate clinical procedures such as clamping of the suprarenal aorta or renal artery during surgery, or the low arterial target pressure during cardiopulmonary bypass, revealed decreases in renal size accompanying renal tissue hypoxia.[44,46-51] Furthermore, explorations detailing the relationship between blood oxygenation level-dependent (BOLD) MRI and renal tissue partial pressure of oxygen (pO_2) revealed correlations between the T_2^* relaxation time and kidney size during aortic occlusion and recovery.[52,53] Recent kidney size assessments in experimental models using noninvasive MRI also included renal pathophysiologies such as experimental diabetes, mutant models mimicking the human manifestation of PKD and renal allograft pathophysiology.[30,54-59]

In vivo renal size assessment requires segmentation of the kidney from noninvasive renal imaging that supports longitudinal studies—a forte of MRI.[15,16] Recognizing this opportunity and the crucial importance of monitoring kidney size changes in the context of renal disease and for gaining new insight into mechanisms of renal pathophysiology, this work examines the feasibility and reliability of longitudinal monitoring of kidney size in MR images of rats using an automated, geometry-based bean-shaped model (ABSM). We hypothesize that this approach enables quantification of acute changes in kidney size in experimental setups mimicking realistic clinical scenarios. To test this hypothesis, sequential in vivo parametric MRI (T_2, T_2^* mapping) was performed in rats undergoing four pathophysiologically relevant interventions: (a) short-term occlusion of the suprarenal aorta, (b) short-term occlusion of the renal vein, (c) short-term increase in renal pelvis and intratubular pressure and (d) bolus injection of an X-ray CM into the thoracic aorta.

2 | METHODS

2.1 | Animal preparation

All investigations were approved by the Animal Welfare Department of Berlin's State Office of Health and Social Affairs in accordance with the German Animal Protection Law, and the experiments were carried out in accordance with the approved guidelines. A total of 34 male Wistar rats (aged 12-13 weeks, body mass 270-300 g, Harlan-Winkelmann, Borchen, Germany) were studied. The animals

had ad libitum access to food (standard diet) and water and were housed under standard conditions with environmental enrichment.

For anaesthesia, urethane (0.2 g/mL in distilled water; 6 mL/kg BM intraperitoneal; Sigma-Aldrich, Steinheim, Germany) was used throughout the surgical preparation and the examination. Surgical preparation included insertion of vascular catheters and invasive probes for quantitative measurements of renal haemodynamics and oxygenation as previously described in detail.[46,52,53,60,61]

Four rat models were employed:

- **Short-term occlusions of the suprarenal aorta:** In the first subgroup of rats (n = 13), an MR safe and remotely operated inflatable occluder was placed around the suprarenal aorta a to perform remotely controlled short-term occlusion of the aorta (Figure 1).[61,62] Studying the impact of this intervention is clinically relevant—several surgical procedures require cross-clamping of the suprarenal aorta,

which if maintained for long periods of time carries the risk of renal ischemia-reperfusion injury.

- **Short-term occlusion of the left renal vein:** In the same first subgroup of rats (n = 13), a MR safe and remotely operated inflatable occluder was placed around the left renal vein to perform remotely controlled short-term occlusion of the renal vein (Figure 1).[61,62] This experimental setup emulates clinical scenarios such as partial nephrectomy, which may also result in renal ischemia-reperfusion injury.

- **Increase in the pressure in the renal pelvis and tubules:** Rats of the second subgroup (n = 5) were instrumented with a ureteral catheter with its tip placed in the left renal pelvis to enable remotely controlled increases in the pressure in the renal pelvis and tubules (Figure 1). The catheter was custom made using polythene tubing (inner diameter 0.4 mm; Portex, Hythe, UK). The catheter was connected to a saline-filled container placed outside the MR scanner. This container was elevated by 41 cm above the level of the rats' kidney to increase the pelvis and tubular pressure
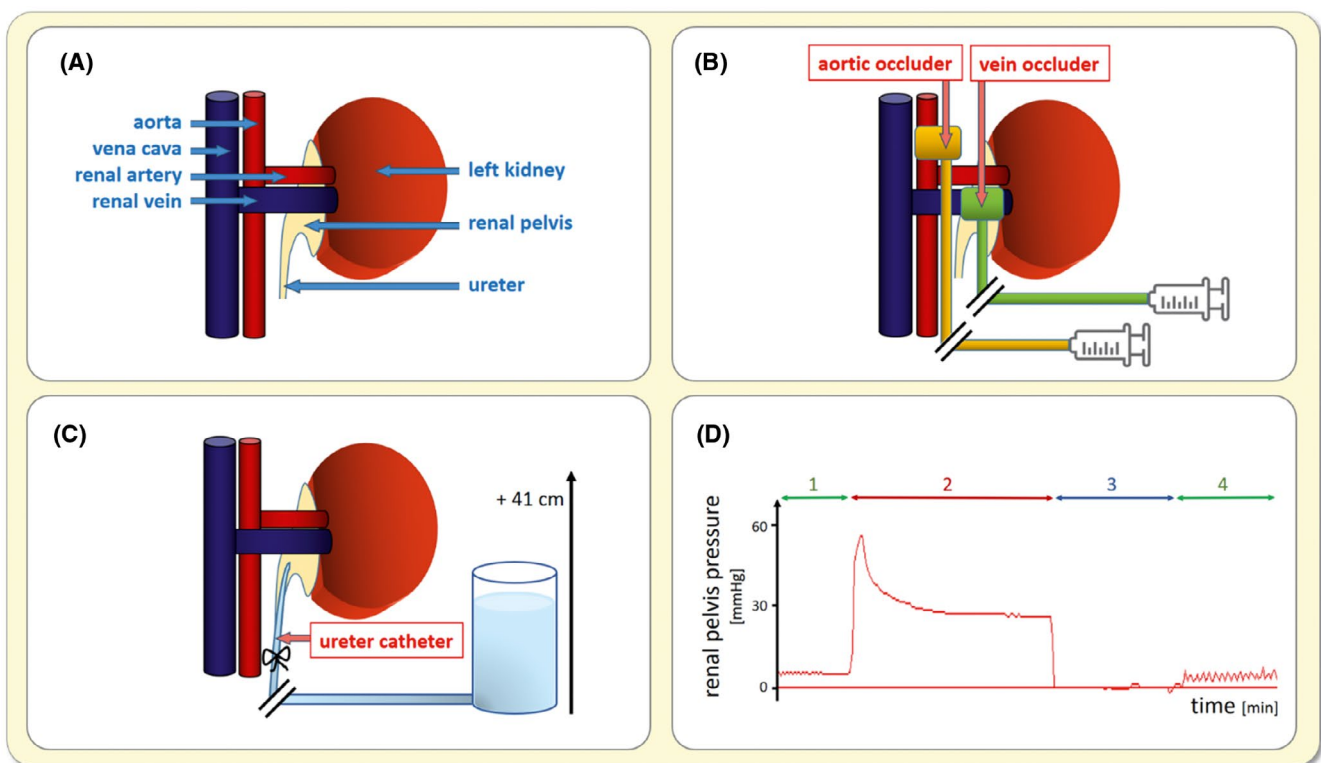

FIGURE 1 Illustration of the experimental models and methods utilized for the reversible pathophysiological interventions. A, Basic scheme depicting the relevant anatomic configuration. B, Inflatable occluders placed around the left renal vein and the suprarenal aorta, connected via catheters (length about 1.5 m) with syringes that were used for remotely controlled short-term occlusions of the respective blood vessel. C, A catheter placed in the left ureter and connected via a catheter (length about 1.5 m) to a container filled with isotonic saline was used for remotely controlled brief increases in renal pelvis and tubular pressures by about 30 mm Hg, achieved by elevating the container 41 cm above the level of the rats' kidneys. D, Pressure trace obtained for the renal pelvis of a rat (pressure transducer: DT-XX, Viggo-Spectramed, Swindon, UK; amplifier & acquisition: TAM-A Plugsys & HAEMODYN, Hugo Sachs Elektronik, March, Germany) recorded (1) during baseline control conditions (green), (2) during pressure increase achieved by injection of saline fluid via the ureteral catheter (red), (3) following disconnection of the catheter to obtain zero pressure for calibration of the pressure measurement (dark blue) and (4) during another control measurement (green). Note that the oscillations observed during control (1) and, even enlarged, during control (4) represent the spontaneous peristaltic contractions of the ureter

by about 30 mm Hg. This experimental intervention is clinically relevant, since upper urinary tract endourologic procedures often cause temporary increases in tubular and intrarenal pressure, and excessive pressures carry the risks of pyelovenous backflow, damage to tubular integrity and hypoperfusion due to compression of intravascular vessels.

- **Intraaortic bolus injection of an X-ray contrast medium:** In the fourth subgroup of rats (n = 9) a catheter was inserted into the left common carotid artery with its tip directed towards the thoracic aorta. This setup was used for bolus administration of the X-ray CM iodixanol (Visipaque, GE Healthcare Buchler, Braunschweig, Germany), which is a highly viscous iodine-containing radiocontrast agent.[63] This experimental setup is an established model of CM-induced AKI.

All surgery and instrumentation procedures were performed in a laboratory outside of the MR scanner room. To transfer the animal into the MR scanner, an in-house designed 3D-printed animal holder adapted to the geometry of the MR scanner bore was used. With this approach the catheters and invasive probes are fixed to stay in position.[52,53,61] In the MR scanner, the rats' core body temperature was monitored by means of a rectal fibre-optic temperature probe (AccuSens, Opsens, Québec City, Canada). Body temperature was maintained at 37℃ with a pad containing circulating warm water (Thermo Haake GmbH, Karlsruhe, Germany) connected to a water bath. Respiration rate was monitored throughout the experiment using a small balloon placed on the chest of the animal (Model 1025, SA Instruments, Stony Brook, NJ, USA). This approach also served for triggering the MRI data acquisition.

2.2 | MRI experiments

All MRI experiments were carried out on a 9.4 Tesla small animal MR system (Bruker Biospec 94/20, Bruker Biospin, Ettlingen, Germany). A linear birdcage radiofrequency (RF) volume resonator (inner diameter: 72 mm; Bruker Biospin) was employed for transmission in conjunction with a curved four-channel surface RF coil array customized for rats (Bruker Biospin) for signal reception.

For geometrical planning and slice positioning, T_2-weighted pilot scans were acquired. Local volume selective shimming of the magnetic field homogeneity on a voxel accommodating the left kidney was conducted using an automatic optimization algorithm based on free induction decay length. Interleaved T_2^* and T_2 mapping was performed with respiratory gated (Model 1025; SA Instruments, New York City, NY, USA) imaging protocols. For T_2^* mapping, a multigradient echo (MGE) technique (TR = 50 ms, number of echoes = 10, first TE = 2.1 ms, interecho time ΔTE = 2.1 ms,

flip angle $\alpha = 16°$, number of averages = 4, $t_{\text{acquisition}}$ = 23 s) was used. For T_2 mapping a multi spin-echo technique (TR = 500 ms, number of echoes = 13, first TE = 6.4 ms, interecho time ΔTE = 6.4 ms, number of averages = 1, $t_{\text{acquisition}}$ = 58 s) was employed. For T_2^* and T_2 mapping a midcoronal oblique image slice was acquired using: in-plane spatial resolution = (226×445) μm^2, FOV = (38.2×50.3) mm^2, matrix size = 169×113 (zero-filled to 169×215), slice thickness = 1.4 mm.

2.3 | Image analysis

First, parametric maps of absolute T_2^* and T_2 were calculated by pixel-wise mono-exponential fitting to the signal intensities of the T_2^*- and T_2-weighted images acquired at different echo times (in-house developed programme; MATLAB, R2010a, MathWorks, Natick, MA, USA). The relaxation times T_2^* and T_2 were chosen over the relaxivities (ie, $R_2^* = 1/T_2^*$ and $R_2 = 1/T_2$), as they allow for a better visualization of changes in the parameter maps for the different kidney regions.

2.4 | Manual segmentation of the kidney by independent observers

The accuracy and precision of the ABSM were evaluated in comparison to 'ground truth' measurements of kidney sizes under baseline physiological conditions, based on a consensus reading of manual segmentation from five independent skilled human observers. For determination of the 'ground truth', manual segmentation of images of the left kidney was applied for baseline physiologic conditions (ie, without any intervention). For this purpose, a total of 60 T_2 maps (n = 20 healthy rats, three time points per rat with a mean Δt = 80 s, variation depending on respiratory gating) obtained under baseline conditions were manually segmented by five independent observers, four observers with 1-8 years of experience in anatomical and/or functional renal MR image analyses in rats and one novice observer.

Prior to renal segmentation, a blinded reading and training session of the five observers was performed, during which all T_2 maps were carefully examined together with the corresponding T_2-weighted images in order to (a) rate and, if necessary, exclude maps according to general image quality and (b) establish clear rules for the observers to adhere to when determining the kidney boundaries. Upon assessing general image quality, 45 T_2 maps obtained from 15 rats were rated as *acceptable* (good imaging quality), 9 T_2 maps from 3 rats were considered *marginal* but feasible and 6 T_2 maps from 2 rats were *unacceptable*. The latter were excluded from further analyses.

Following assessment of the image quality, the five observers agreed upon the following rules for manual segmentation of the left kidney, based upon the T_2-maps and the corresponding T_2-weighted images:

1. Disregard details of the kidney tissue boundary in the region of the renal hilus, where the geometrical configurations of the papilla (renal tissue) and the renal pelvis, together with their very close proximity, results in partial volume effects in the majority of cases, thus making accurate designation of the tissue boundary almost impossible. Instead, draw a straight line that connects the outermost points of the upper and lower medial curvatures, as outlined in Figure 2A.

2. When encountering indentations of the tissue boundary that may result from the invasive probes, view all individual T_2-weighted images. If the indentation is present in the majority of T_2-weighted images, exclude the indentation area, as illustrated in Figure 2B,C.
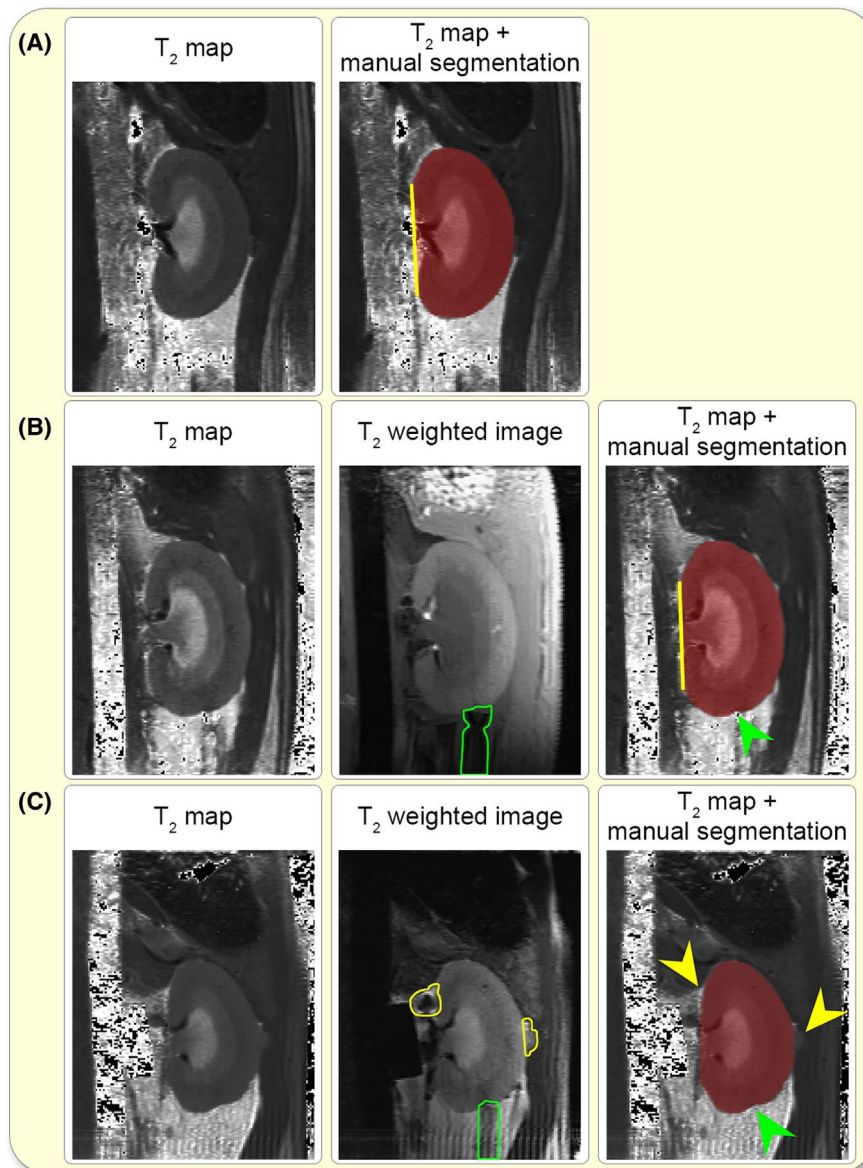

FIGURE 2 Illustration of the consensus rules employed for manual segmentation of the kidney by examples of T_2 maps, selected individual T_2 weighted images derived from the data set used for T_2 map calculation, and T_2 maps with resulting manual segmentations indicated by transparent dark red overlays. A and B, Considering the spatial conditions in the area of the renal hilus, a straight line (yellow) was drawn to connect the outermost points of the upper and lower medial curvatures to represent the segmentation border here. B and C, Where indentations of the renal tissue (eg, by invasive probes—green outlines) were observed, these areas were excluded (green arrows), when confirmed in (the majority of) the individual T_2 weighted images. C, Where distortions of the kidney boundary (possibly related to air or to fat-induced artefacts—yellow outlines) were observed in T_2 maps and in (the majority of) the individual T_2 weighted images, kidney borders were drawn according to the typical curvature of the kidneys, thereby excluding these distortions (yellow arrows)

3. When encountering distorted kidney boundaries due to susceptibility artefacts or air cavities, view all individual T_2-weighted images. If air or similar voids are visible in the majority of T_2-weighted images, draw the boundary so that it follows as closely as possible the normal curvature of the kidney, as depicted in Figure 2C.

Following the training session, each of the observers independently determined the cross-sectional area (measured as number of voxels) of the midslice coronal view of the left kidney by manually segmenting the boundaries of the kidney using the software ITK-SNAP (www.itksnap.org).[64] No time limits were set for this process. Two of the observers, one with 8 years of experience in renal MRI in rats, the other one a novice, independently recorded the total time required for manual segmentation of a single T_2 map, including data import and file handling steps, and visual inspection of the T_2-weighted images, according to the above rules. Following segmentation, renal boundaries were saved in ITK-SNAP as NIFTI image files.

2.5 | Consensus manual segmentation of the kidney

Following the independent manual segmentation procedure, a consensus segmentation involving all observers was conducted for determining the 'ground truth'. For this purpose, the median voxel count of the five observers was computed first for each animal and time point. To set a starting point for the consensus segmentation, the observers used the renal segmentation of one observer whose segmentations corresponded closest to the median values. Subsequently, each of the 54 T_2 maps was presented to all observers in ITK-SNAP together with a transparent overlay of the area determined as belonging to the kidney (Figure 2). Training was performed using two T_2 maps as examples: one T_2 map with very good image quality (classified as *acceptable*), one T_2 map with lower image quality (classified as *marginal*). From these training data, a consensus was reached regarding the inclusion/exclusion of voxels with apparent partial volume effects. For the remaining consensus reading, renal segmentation T_2 maps—but not the corresponding T_2 weighted images—were used. During the consensus reading, the observers remained blinded to the individual T_2 map number, the animal identification, the numerical kidney size derived from the independent renal segmentation and the number of voxels of the overlay. Upon presentation of each T_2 map along with the corresponding transparent overlay, all observers agreed in real time if it was necessary to add or delete certain voxel(s) to/from the overlay, in order to improve the accuracy of the renal boundaries, whereupon a consensus on the total area

assigned as renal tissue was reached. Changes were adopted in real time using ITK-SNAP. A time limit of 90 s was set for the consensus renal segmentation of each T_2 map.

2.6 | Automatic segmentation of the kidney using the bean-shaped model

The midslice cross-sectional area of the kidney (hereafter referred to as 'renal size') was calculated using a bean-shaped model. An analytic function describing the shape of the kidney was used and fitted to the edges found in the MR images. The function in Equation 1 was found to describe the shape of a coronal slice of rat kidneys very well:

$$r = A \left(a\sin^3 \left(\theta - \theta_0 \right) + b\cos^3 \left(\theta - \theta_0 \right) + 0.1\sin^5 \left(\theta - \theta_0 + \frac{\pi}{4} \right) \right) \tag{1}$$

where r, curve describing the kidney border as a function of the polar angle θ; A, kidney size parameter; a, b, kidney anisotropy parameters; $b = \sqrt{2 - a^2}$; θ_0, rotation angle.

Two additional parameters for the position and one additional parameter to stretch or contract one of the axes were included in the model after transferring the shape to Cartesian coordinates using the MATLAB function *pol2cart*. These six parameters were optimized for every MR image for automatic segmentation of the kidney. An example of the shape of the function overlaid onto the corresponding T_2 map is depicted in Figure 3.

The objective function (Equation 2) of the optimization was based mainly on the edges detected in the T_2 and T_2* maps and in the T_2 and T_2* weighted images (TE = 2.1 ms and TE = 12.6 ms) and on the uniformity of T_2 and T_2* in the renal cortex and in the outer medulla. Edge detection was performed with the MATLAB function *edge* using the Canny method. For renal segmentation of the T_2* data, the edge images derived from the T_2* map and from two T_2* weighted images (TE = 2.1 ms and TE = 12.6 ms) were averaged. For renal segmentation of the T_2 data, an average over the edge images derived from the T_2 map and the first two singular vectors of all images was found to work best.

$$d = \sqrt{\frac{s_{circ} \sum d_{edge}}{c \sum I_{edge}}} \tag{2}$$

where d, deviation metric minimized; s_{circ}, average standard deviation of the T_2 or T_2* values on rings 3 to 14 voxels below the current kidney boarder; d_{edge}, distance between the current kidney boarder and the closest point with an edge value of more than 0.3; I_{edge}, linearly interpolated value of the edge image at
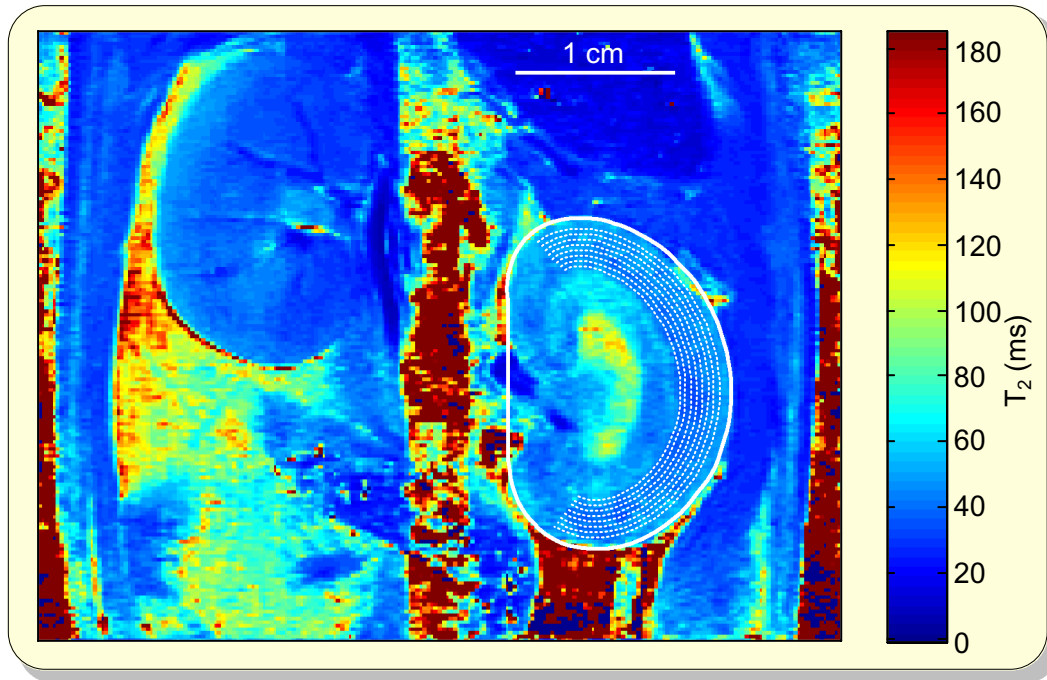
FIGURE 3 Illustration of the kidney shape function obtained from the bean-shaped model overlaid onto the corresponding T_2 map. The dashed white lines below the kidney surface indicate the lines on which the standard deviation was computed in order to describe the homogeneity within the kidney

all points of the current kidney boarder; c, circumference of the kidney (used to exclude results that include only parts of the kidney).

As shown in Equation 2, three factors were included in the objective function to be minimized. First, the homogeneity of the T_2 or T_2^* values in the cortical and outer medullary region was evaluated as the standard deviation of the values found below the renal surface. Second, the distances to the next edge in the direction orthogonal to the current boarder were determined. Third, the edge image values were interpolated to the points of the kidney boarder and summated. Fourth, the results were scaled by the square root of the circumference of the kidney in order to slightly disfavour results that included only parts of the kidney.

For the first baseline image of each animal obtained under physiological conditions without any intervention, predefined fixed values for the variables of Equations 1 and 2 ($A = 61$, $\theta_0 = 0°$, $Pos_x = 190$, $Pos_y = 90$, X-stretch = 105%, $a = 100\%$) were used as starting parameters for the kidney shape function. The size parameter A and the position parameters are in units of voxel width. For all other images, the results of the previous optimization were used as starting values. As the first step of each optimization procedure, the kidney position was optimized alone, keeping the other parameters fixed. Afterwards, a free optimization was performed using the active-set algorithm implemented in the MATLAB *fmincon* function. The parameters were constrained to stay in a reasonable range (eg, $0.87 < a < 1.13$). In order to leave potential local minima, the optimization was repeated 16 times starting from the current optimum disturbed by Gaussian random numbers with the sigma equal to 1% of the parameter value. The best reached optimum was used.

After optimizing the kidney shapes for all images, an additional refinement step was included that optimized the lines connecting the current optimum of a given image with the optima of the 20 images closest in time (*fminbnd* MATLAB function) followed by a free optimization (*fmincon* MATLAB function). Again, the best solution was kept. In order to quantify the reproducibility of the fit result, this procedure was performed five times for each animal.

2.7 | Longitudinal quantification of renal size changes upon pathophysiological interventions

For the quantification of changes in kidney size using the ABSM approach, reversible pathophysiologically relevant interventions were performed.[27,29,46,62] These included brief periods of (a) occlusion of the suprarenal aorta (which decreases renal size), (b) occlusion of the left renal vein (which increases renal size) and (c) increased renal pelvis and tubular pressure (which increases renal size). Occlusion of the suprarenal aorta and the renal vein was done before and after administration of the ultrasmall superparamagnetic iron oxide (USPIO) preparation, ferumoxytol, in order to demonstrate the efficacy of the ABSM approach in the context of substantial reductions in MR signal intensity and image

contrast. Finally, the ABSM approach was applied to quantify changes in kidney size upon a nonreversible intervention, that is, injection of an X-ray CM into the thoracic aorta, which is expected to result in an increase in kidney size.

The following procedures were performed in rats in the first subgroup that had been equipped with remotely operated inflatable occluders placed around the suprarenal aorta and the left renal vein:

1. control baseline period of about 10 min
2. short-term occlusion of the aorta
3. 10-min recovery period
4. short-term occlusion of the renal vein
5. 10-min recovery.

The average duration of the short-term occlusion of both the aorta and the renal vein was 3.8 ± 0.3 min, depending on respiratory gating. Time of flight (TOF)-based MR angiography was performed immediately after inflation and deflation of the respective occluder to confirm the successful occlusion and reperfusion of the aorta or vein. Following this first set of vascular occlusions, the USPIO preparation, ferumoxytol (Feraheme, AMAG Pharmaceuticals, Inc, Lexington, MA, USA, 2 mg Fe/kg BM) was intravenously injected as previously described.[62] The administration of ferumoxytol does not have any measurable effects on renal physiology at doses up to 41 mg Fe/kg BM in rats and does not significantly alter the control of renal haemodynamics and oxygenation, as studied by aortic occlusion and hypoxia.[48] However, ferumoxytol substantially reduces the signal intensity due to T_2 and T_2^* shortening and affects the image contrast.[62] About 10 min after ferumoxytol injection, a second set of vascular occlusions was performed according to the same schedule as with the first one. Occlusion of the suprarenal aorta and occlusion of the left renal vein was successfully performed in n = 12 rats, prior to and after injection of ferumoxytol.

The following workflow was performed in the second subgroup of rats that were equipped with the ureteral catheter:

1. control baseline period of about 10 min
2. short-term increase of renal pelvis and tubular pressure (average duration 9.2 ± 0.4 min, depending on respiratory gating)
3. 10-min recovery.

Elevating the saline-filled container connected to the ureteral catheter by 41 cm above the level of the kidney increases renal pelvis and tubular pressure by about 30 mm Hg. This pressure level was chosen because comparable increases in tubular pressure were measured during upper tract endourologic procedures in human patients and within 10 min of acute ureteral obstruction in rats during osmotic diuresis. The pressure level of 30 mm Hg is below the threshold pressure for pyelovenous backflow and renal damage.[27,29] The pressure increase was successfully performed in n = 5 rats.

An established model of X-ray CM-induced AKI[41-43,65] was employed in a third subgroup of rats instrumented with a carotid artery catheter:

1. control baseline period of about 10 min
2. injection of a prewarmed (37℃) X-ray CM (iodixanol of 320-mg iodine/mL, GE Healthcare Buchler, Braunschweig, Germany) as a bolus of 1.5 mL (equivalent to approximately 1.5-mg iodine/g of BM) into the thoracic aorta. Injection of a 0.2-mL isotonic saline chaser bolus to account for the catheter dead space.

The response was monitored for 60 min after CM administration in n = 9 rats.

2.8 | Statistical analysis

Interobserver variability in the voxel counts of kidney segmentations was evaluated using a correlation matrix of Pearson correlations for all pairwise combinations of the five independent observers. Histograms showing the distribution of counts for each observer were plotted, together with the scatterplot for each pair of observers, along with a locally estimated scatterplot smoothing (LOESS) line. The level of agreement among all observers combined was evaluated using the intraclass correlation coefficient (ICC), considering the mean value of the five observers in a two-way random effects model. For both Pearson and ICC, each individual T_2 map was considered as an independent sample (n = 54). The ICC analysis was then repeated, considering the consensus renal segmentation as an additional independent observer. The accuracy of each observer is defined as the magnitude of the correlation with the consensus reading of the manual segmentations, which served as the 'ground truth' value of the renal size.

Intra-observer variability in the voxel counts of kidney segmentations was analysed by determining the percent deviation in the area determined from the three consecutive T_2 maps acquired for each animal during the baseline period (total duration $\approx$ 6 min, during which no substantial physiological variations were assumed).

Intrasubject variability was assessed by calculating the coefficient of variation (CV) among the three replicate scans of each individual animal (n = 18), as assessed by each of the five observers independently and in the consensus renal segmentation. The median CV of all animals was compared among the five observers, the consensus renal segmentation and the renal segmentation with the bean-shaped model using the nonparametric Friedman repeated-measures ANOVA,

with Dunn's post hoc comparison. The CV of the replicate scans also served as a metric of the precision of each independent observer and of the automated segmentation method.

Changes in renal size during the interventions were assessed by two-factor repeated measures ANOVA followed by Dunnett's post hoc test.

Statistical analysis was done using the statistical computing environment R v.3.3.4 (https://www.R-project.org) and GraphPad Prism v.5.01 (GraphPad Software, Inc). *P*-values <.05 were considered statistically significant.

3 | RESULTS

3.1 | Manual segmentation of the kidney by independent observers

The average time required for manual segmentation of a given T_2 map, including visual inspection of the corresponding T_2-weighted images when necessary (about one third of the cases), was 16 ± 8 and 17 ± 5 min (mean $\pm$ standard deviation, SD) for the experienced and the novice observer, respectively. Following independent manual segmentation, the interobserver variability of the renal size was analyzed. For this purpose, (a) the mean value, SD, range (minimum to maximum value), median and percent variations (range/mean*100 and [mean − individual reader]/mean*100) for each individual T_2 map and (b) the mean, SD and range of all 54 T_2 maps were computed. The mean number of voxels assigned to the kidney area averaged over all 54 maps was 4205 ± 339 (mean $\pm$ SD) voxels, corresponding to an area of 221 ± 18 mm². The percent variation among the observers averaged over all T_2 maps amounted to $7.3 \pm 2.8\%$, with a maximum variability among readers in an individual T_2 map of 14.6% and a minimum variability in another individual T_2 map of 3.7%. Since the interobserver variability obtained for the nine T_2 maps (3 rats) designed as *marginal* according to their general image quality was well within the range of those designated as *acceptable*, these data were not excluded from the analysis. Averaged over all 54 maps, the mean percentage deviation of individual observers from the mean value of all five observers ranged from −3.2% to 3.0%, with maximum deviations of individual observers from the group mean in a given map of −7.0% and 8.7%, respectively.

To evaluate the interobserver variability in the voxel counts of the renal segmentations, we plotted the pairwise correlations among all five observers, as well as the consensus reading, which was considered as an additional observer. The distribution of voxel counts for each observer is depicted as a histogram with marginal density plots on the diagonal of the correlation matrix (Figure 4). The correlations for each pair of observers are shown in the lower panels of the figure

together with a LOESS fit line. The Pearson correlation coefficients for each pair of observers were all significant with values of $r^2 > .91$ (Figure 4). The ICC for the combination of all five observers was 0.96 ($P = 2.3 \times 10^{-117}$).

For analysis of the intra-observer variability as a measure of precision, for each animal, the percent deviation of the renal size determined from the three consecutive baseline T_2 maps from the mean value of these three T_2 maps was calculated. Averaged over all 18 rats, the precision as indicated by the mean SD of all five readers was 0.6%; the observer with the highest variability had a mean SD over all 18 rats = 1.0% (range −2.8% to 2.5%), whilst the observer with the lowest variability had a mean SD over 18 rats = 0.2% (range −0.5% to 0.6%).

To evaluate the intrasubject variability, the CV for the three replicate scans for each animal was calculated. CVs are displayed for each rat, as assessed by the five observers and the consensus reading (Figure 5). The results indicate low variability among replicate scans; only 5/108 (ie, from n = 18 subjects times n = 5 observers) subjects had a CV >2%, demonstrating a high degree of precision of the independent observers. Figure 5 illustrates that no individual subjects yielded a greater CV consistently for all observes. There were no 'problematic' animals with excessive differences among replicate scans.

3.2 | Consensus manual segmentation of the kidney

For the consensus manual segmentation of the kidney, the median voxel count of the five independent observers was computed for each T_2 map. In 35 of the 54 cases, the median corresponded to values from the same observer (values of the other observers constituted the median in 10, 5, 3 and 1 cases, respectively). The mean number of voxels averaged over all 54 maps obtained by the consensus conference was 4199 ± 322, corresponding to an area of 221 ± 17 mm². The consensus segmentation resulted in a negligible overall percentage difference versus the mean and median values of the five independent observers (mean $0.2 \pm 1.0\%$ and mean $−0.2 \pm 0.9$, respectively). As shown in Figure 4, upon including the consensus segmentation as an additional observer, the strength of the ICC increased (0.98, $P = 2.2 \times 10^{-157}$). The analysis of the intra-observer and intrasubject variabilities obtained by the consensus renal segmentation averaged over all 18 rats yielded a SD of 0.8%. For individual rats, the percentage variation ranged from −2.1% to 2.3%. The consensus reading can be considered as the 'ground truth'. The fact that each of the independent observers showed a correlation coefficient with the consensus reading ≥0.95 indicates a high degree of accuracy (Figure 4). Whilst there were significant differences in the mean CV in renal size from replicate scans
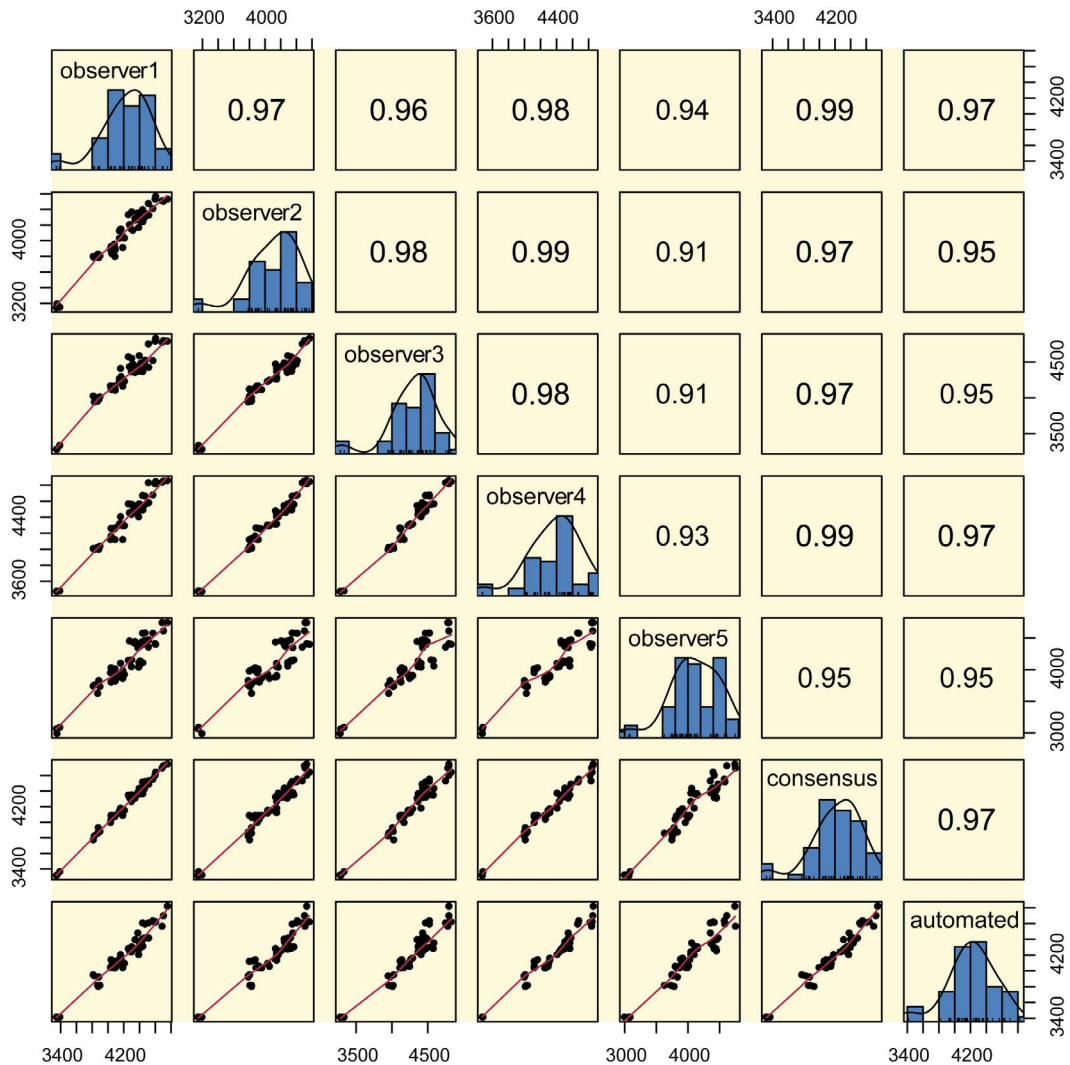
FIGURE 4 Correlations of renal size measurements among all observers. The distribution of the voxel counts for each independent observer, for consensus segmentation, and for renal segmentation using the automated bean-shaped model is displayed in histograms with marginal density plots along the diagonal. Scatterplots showing the pixel count for each data set are shown along with LOESS lines of best fit, for each pair of observers (lower left panels); Pearson correlation coefficients are shown in the upper right panels

among the observers, in almost all cases the CV was <2%, indicating a high degree of precision (Figure 5). To conclude, the consensus reading of the five independent manual renal segmentations provided a stable 'ground truth' as illustrated by the CVs highlighted in Figure 5.

3.3 | Segmentation of the kidney using the bean-shaped model

Automatic kidney segmentation was performed for all data sets. The ABSM-based kidney segmentation required less than 14 s per image using a standard consumer PC. The SD of the renal size resulting from the successive segmentations of the same image was found to be on average 0.6% for the T_2 scans and 1.3% for the T_2* scans. The SD of the determined areas of the three successive baseline scans was on

average 0.6% of the total size for T_2 scans and 1.6% for T_2* scans. These results coincide well with the intra-observer variability found in the manual segmentation. The correlation of the areas found by automated segmentation with the consensus manual reading ('ground truth') yielded a Pearson correlation coefficient of $r^2 = .97$ (Figure 4). The assessment of the intrasubject variability of the segmentation using the ABSM yielded a CV similar to that obtained from the consensus segmentation or from individual manual segmentation, indicating that the bean-shaped model had an equivalent precision (Figure 5). In conclusion, automated kidney segmentation using the ABSM affords an ~70-fold increase in segmentation speed whilst maintaining the accuracy and precision of manual segmentation by a human observer. This renders bean-shaped model-based segmentation suitable for time-resolved analysis and longitudinal monitoring of renal size.
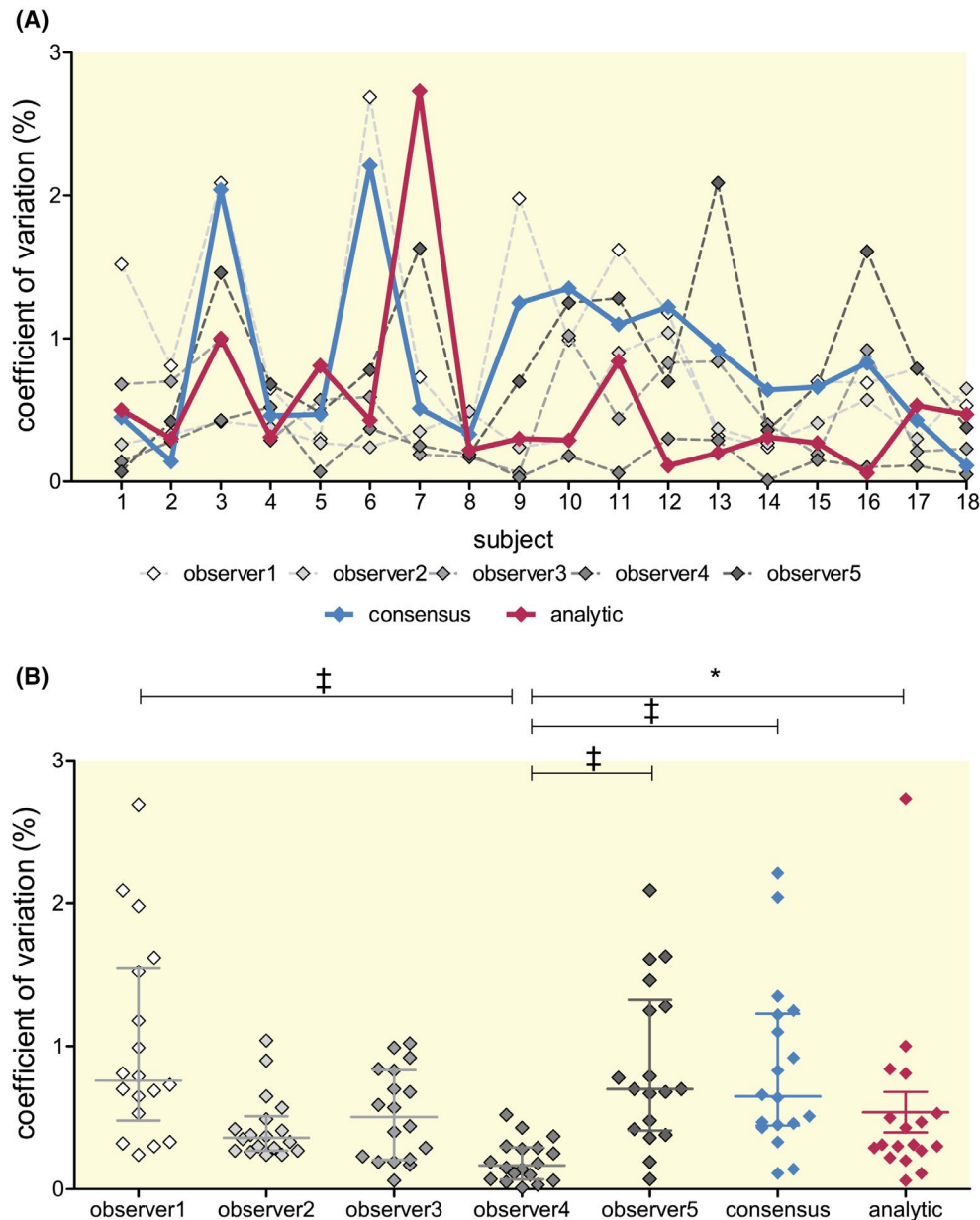
FIGURE 5 A, Intrasubject variability by animal. The coefficient of variation (CV) was calculated from three replicate baseline scans of each rat. Each point represents one subject, as measured by each of the five observers (grey colours correspond to observers). The coefficients of variation of the consensus renal segmentation are shown in blue. The coefficients of variation derived from renal segmentation using the automated bean-shaped model are shown in read. B, Intrasubject variability by observer. Each point represents the CV from three replicate T_2 maps acquired during baseline conditions of each individual animal (median $\pm$ interquartile range), plotted for all observers, including the consensus renal segmentation (blue) and the renal segmentation using the automated bean-shaped model (red) as additional observers. There were significant differences in the median CV for one observer versus two other observers and versus the consensus reading as well as the analytic approach (nonparametric Friedman repeated-measures ANOVA followed by Dunn's post hoc test: *$P < .05$, ***$P < .001$)

3.4 | Renal size changes upon short-term occlusion of the suprarenal aorta or the renal vein

The ABSM approach was applied to detect and quantify changes in renal size in response to dedicated pathophysiologically relevant interventions. Upon occlusion of the suprarenal aorta, there was a significant decrease in renal size

($P < 2.2 \times 10^{-16}$, two-factor repeated measures ANOVA). Renal size as obtained from T_2 maps was reduced from 220 ± 14 to 205 ± 14 mm^2 (mean $\pm$ SD) approximately 2 min following the occlusion (-7.2%, $P < .0001$, Dunnett post hoc test) and remained significantly reduced during the occlusion (Figure 6). After termination of the occlusion, renal size returned to baseline levels within about 9 min (217 ± 16 mm^2, $P = .53$ vs baseline prior to occlusion, Dunnett test, Figure 6).
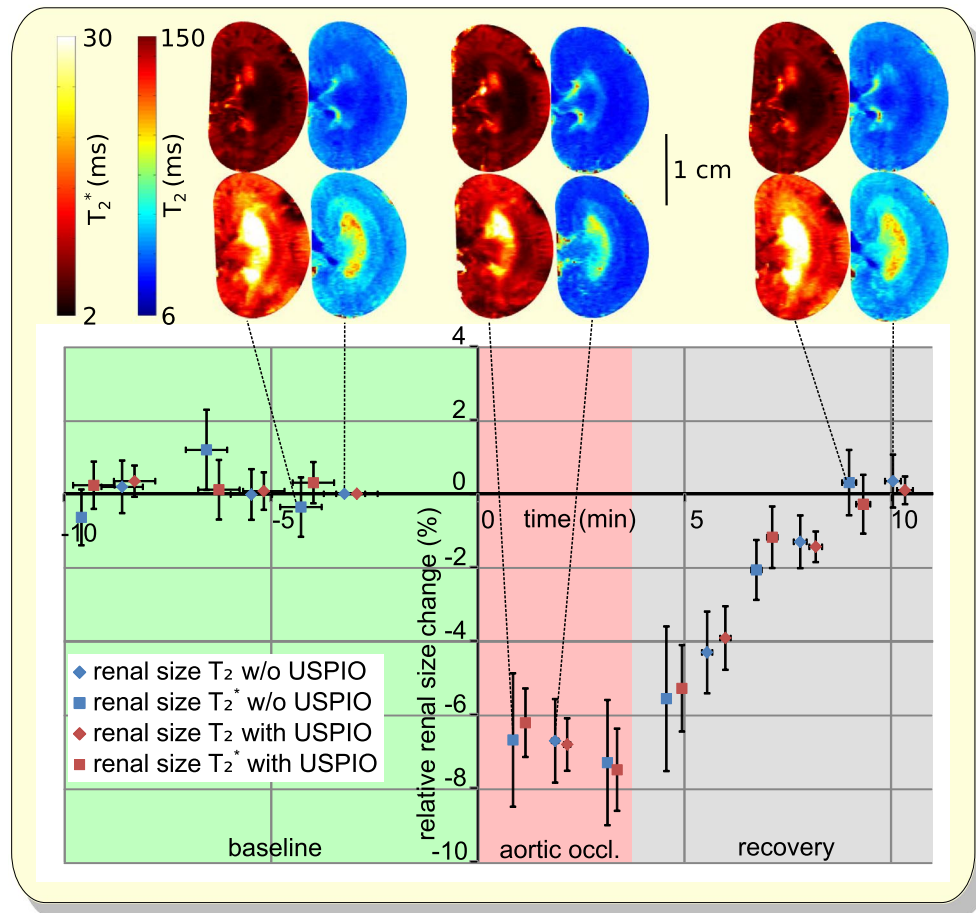
FIGURE 6 Temporal evolution of relative changes in renal size during occlusion of the suprarenal aorta and upon cessation of the occlusion derived from T_2 and T_2* maps of the kidney using the automated bean-shaped model. The intervention was performed twice, that is, before (blue symbols) and after (red symbols) administration of the ultrasmall superparamagnetic iron oxide (USPIO) preparation, ferumoxytol. The symbols were jittered by 9 s to the left or right to avoid overlap. Data obtained for n = 12 rats are given as mean ± SEM of changes related to the last T_2 maps obtained before the start of the occlusion of the suprarenal aorta at time 0. Exemplary colour-coded renal T_2* and T_2 maps (colour scales in milliseconds) are shown above for the cases before (lower row) and after (upper row) administration of the USPIO

A similar time course of changes in renal size was obtained from T_2* maps (Figure 6).

Following the aortic occlusion, sufficient time was granted to ensure that renal haemodynamics and oxygenation as well as kidney size had returned to the initial baseline levels ($P = .99$, repeated-measures ANOVA with Dunnett test), before applying the next intervention, that is, venous occlusion. Occlusion of the left renal vein induced a significant increase in renal size ($P < 2.2 \times 10^{-16}$, two-factor repeated measures ANOVA). Renal size obtained from T_2 maps increased from 221 ± 13 to 230 ± 14 mm^2 approximately 2 min following the start of the occlusion ($+4.5\%$, $P < .001$, Dunnett test, Figure 7). After termination of the occlusion, renal size returned to baseline levels very quickly even prior to our first T_2 scan 2 min after the occlusion was released (219 ± 13, $P = .49$ vs baseline, Dunnett test, Figure 7). Similarly, T_2* maps showed a significant increase in renal

size, changing from 224 ± 15 to 234 ± 17 mm^2 ($+4.5\%$, $P < .001$) approximately 1 min following occlusion, which remained significantly increased during the occlusion and then returned back to baseline levels after termination of the occlusion (Figure 7).

Administration of the USPIO preparation, ferumoxytol, did not have a significant effect on renal size, obtained by either T_2 or T_2* maps ($P = .67$, $P = .77$, respectively, repeated measures ANOVA, Figure 8). Following ferumoxytol administration, the suprarenal aortic and renal venous occlusions were repeated. Sufficient time was granted to ensure that renal haemodynamics, oxygenation and renal size had returned to the initial baseline levels at the start of the experiment, prior to any intervention (baseline post-ferumoxytol aortic occlusion vs initial baseline: $P = .99$, $P = .44$, T_2 and T_2* maps, respectively; baseline post-ferumoxytol venous occlusion vs initial baseline: $P = .99$,
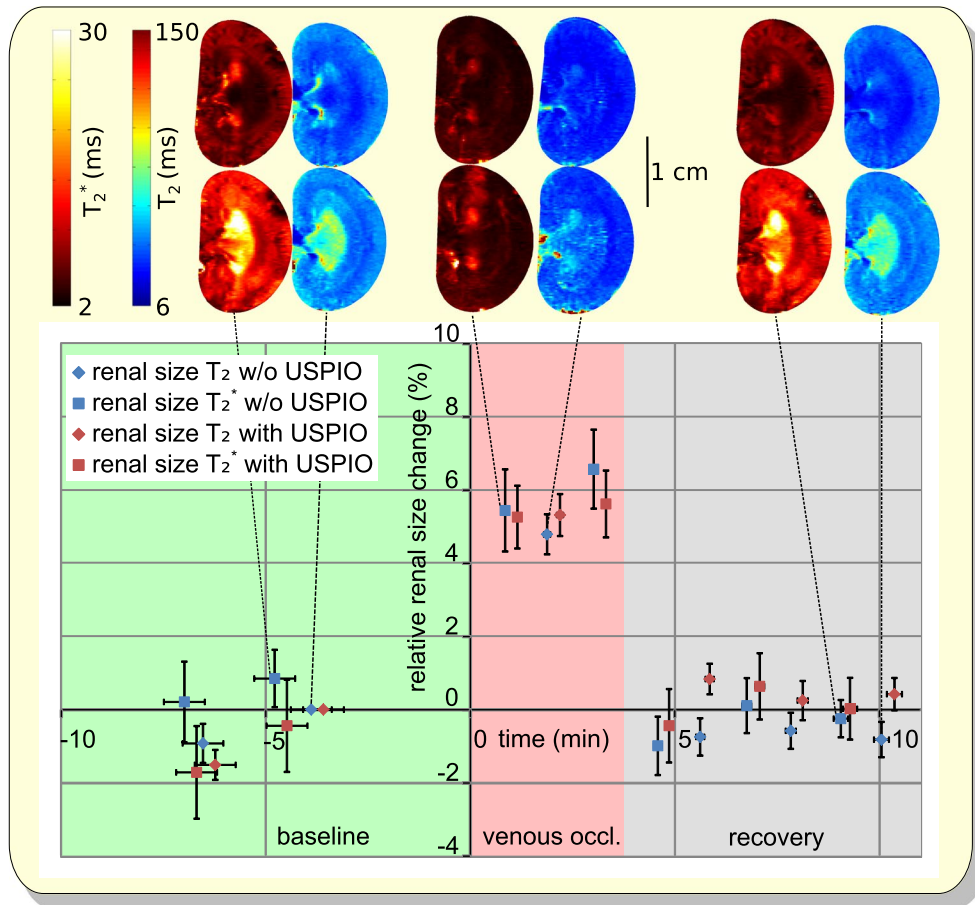
FIGURE 7 Temporal evolution of relative changes in renal size during the occlusion of the left renal vein and upon cessation of the occlusion derived from T_2 and T_2^* mapping of the kidney using the automatic bean-shaped model. The intervention was performed twice, that is, before (blue symbols) and after (red symbols) administration of the ultrasmall superparamagnetic iron oxide (USPIO) preparation, ferumoxytol. Data obtained for n = 12 rats are given as mean $\pm$ SEM of changes related to the last T_2 maps obtained before the start of the occlusion of the left renal vein at $t = 0$ min. Exemplary colour-coded renal T_2^* and T_2 maps (colour scales in milliseconds) are shown above before (lower row) and after (upper row) administration of the USPIO. The symbols were jittered by 9 s to the left or right to avoid overlap

$P = .97$, T_2 and T_2^* maps, respectively, repeated-measures ANOVA, Dunnett post hoc test). Ferumoxytol did not compromise the automated bean-shaped segmentation: the changes in renal size quantified during the second round of pathophysiological interventions with ferumoxytol were almost identical to those in the first round without ferumoxytol. Thus, aortic occlusion following ferumoxytol administration induced a significant reduction in renal size (from 220 ± 15 to 205 ± 13 mm², -7.2%; 226 ± 9 to 209 ± 14 mm², -8.0%, $P = .0001$, $P = .005$, T_2 and T_2^* maps, respectively, Figure 6). Similarly, a significant increase in renal size was detected following the postferumoxytol renal venous occlusion. Renal size increased from 222 ± 15 to 234 ± 14 mm² $(+5.3\%)$ and from 222 ± 15 to 236 ± 17 mm² $(+5.9\%$, $P < .001$, $P = .007$, T_2 and T_2^* maps, respectively, repeated-measures ANOVA, Dunnett post hoc test, Figure 7).

3.5 | Renal size changes upon pelvic/tubular pressure increase

Kidney size increased significantly upon experimentally increased pressure in the renal pelvis and tubules ($P = 3.3 \times 10^{-6}$, repeated-measures ANOVA, Figure 9). Renal size obtained from T_2 maps with the ABSM increased from 205 ± 17 to 209 ± 17 mm² $(+2\%)$ approximately 2 min following the start of the pressure intervention ($P = .0033$, Dunnett post hoc test). Renal size remained significantly elevated throughout the intervention ($P < .001$) and recovered to baseline levels approximately 6-7 min after cessation of the pressure increase (206 ± 18 mm², $P = .81$ vs pre-intervention, Dunnett post hoc test, Figure 9). Renal size determined from T_2^* maps showed the same pattern, increasing from 218 ± 22 to 219 ± 24 mm² $(+1\%$, $P = .0032)$ approximately 2 min following the intervention, remaining significantly increased
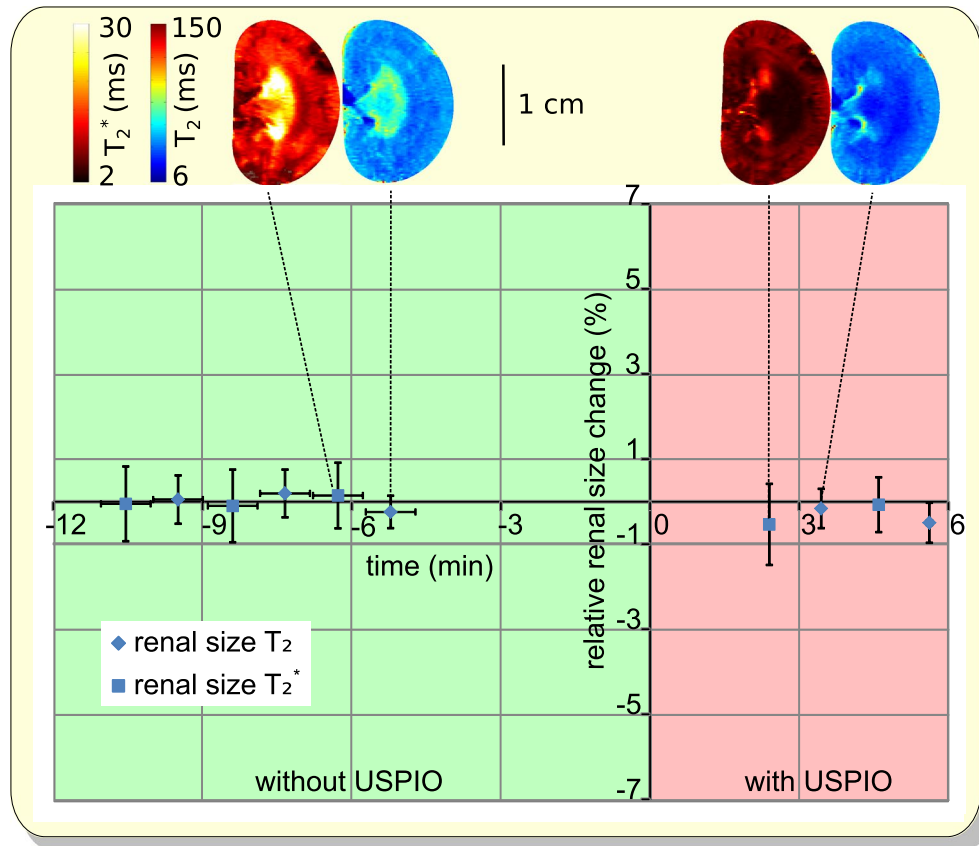
FIGURE 8 Temporal evolution of relative changes in renal size upon intravenous injection of the ultrasmall superparamagnetic iron oxide (USPIO) preparation, ferumoxytol derived from T_2 and T_2* mapping of the kidney using the automated bean-shaped model. Data obtained for n = 13 rats are given as mean ± SEM of changes related to the mean kidney size of the six last T_2 maps obtained before the start of the USPIO injection at time 0 to minimize the influence of measurement uncertainty on the graph. Exemplary colour-coded renal T_2* and T_2 maps (colour scales in milliseconds) are shown above

throughout the intervention ($P = .00015$) and recovering to baseline levels after cessation of the pressure increase (215 ± 20, $P = .81$ vs pre-intervention, repeated-measures ANOVA with Dunnett post-hoc test, Figure 9).

3.6 | Renal size changes upon X-ray CM-induced AKI

Administration of the X-ray CM iodixanol induced a significant and sustained increase in renal size ($P = 3.3 \times 10^{-6}$, repeated-measures ANOVA, Figure 10). Renal size determined from T_2 and T_2* maps using the ABSM increased from 192 ± 33 and 202 ± 31 mm^2, respectively, to 206 ± 29 and 212 ± 29 mm^2 (+6%, $P < .001$ and +5%, $P = .005$, respectively, Dunnett post-hoc test, Figure 10). This increase peaked approximately 7 min after administration, at +9% and +8% ($P < .001$, $P < .001$, T_2 and T_2*, respectively) and remained significantly elevated over baseline size for the whole observation period of 60 min following the administration ($P < .001$, $P < .001$, T_2 and T_2*, respectively, Dunnett post-hoc test, Figure 10).

4 | DISCUSSION

This study demonstrates the feasibility of automatic segmentation of renal MR images using a geometry-based bean-shaped model to monitor and quantify pathophysiologically relevant changes in kidney size in small rodents. We used an experimental paradigm to mimic clinical scenarios, inducing changes in renal size using occlusion of the suprarenal aorta and the renal vein, increase in renal pelvis and tubular pressure and administration of an X-ray contrast medium, whilst acquiring serial MRI scans. These scans were then analyzed using the automated segmentation with the bean-shape model, which required less than 14-s processing time per T_2 or T_2* map, yielding a ~70-fold increase in segmentation speed using a standard consumer PC compared to the time required by trained human observers with an average segmentation time of 16-17 min per T_2 map. Crucially, the automated bean-shaped model (ABSM) showed a high level of both accuracy and precision, equivalent to that of the human observers. This demonstrates that the ABSM-based segmentation is suitable for time-resolved analysis, longitudinal monitoring and quantification of renal size in rats.
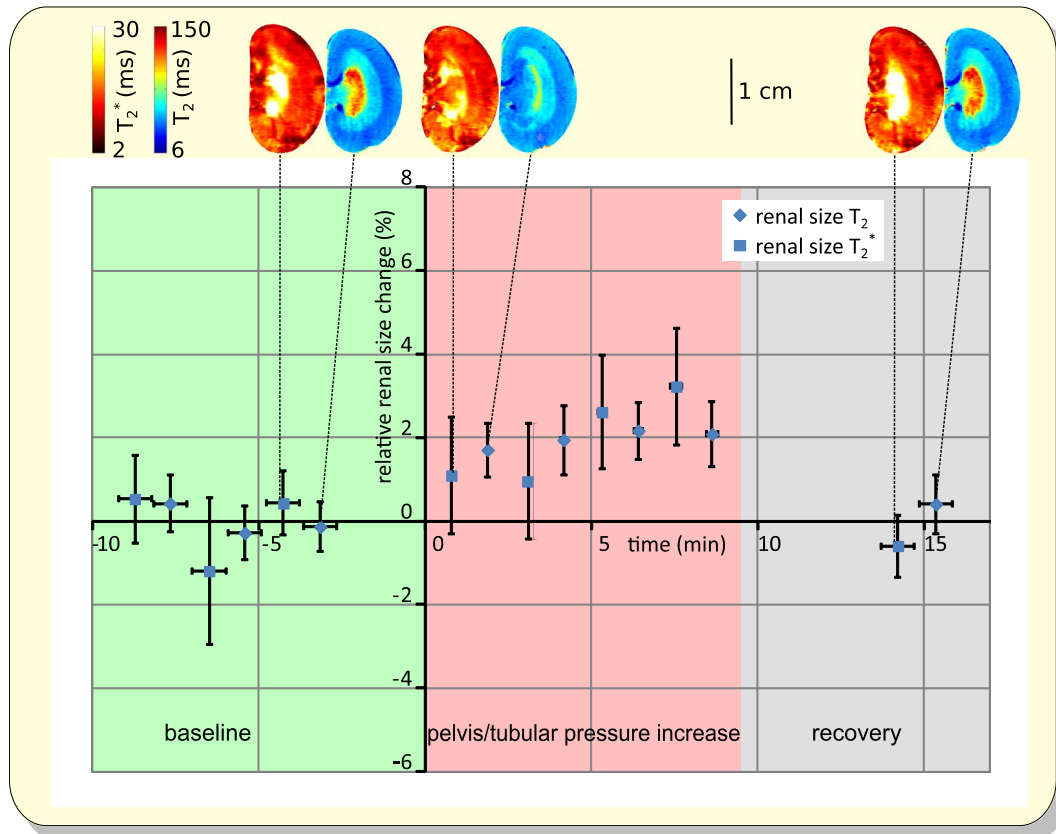
FIGURE 9 Temporal evolution of relative changes in renal size upon renal pelvis/tubular pressure increase derived from T_2 and T_2* mapping of the kidney using the automatic bean-shaped model. Data obtained for n = 5 rats are given as mean ± SEM of renal size changes relative to the last T_2 maps obtained before the onset of pelvis/tubular pressure increase at $t = 0$ min. Exemplary colour-coded renal T_2* and T_2 maps (colour scales in milliseconds) are shown above

Renal size assessment requires accurate segmentation of the kidney from images. Manual renal segmentation is time-consuming and highly prone to observer bias. This poses a major impediment for dynamic and longitudinal clinical and experimental studies and severely limits the potential for renal size assessment in translational research and routine clinical practice.[66] These constraints can be minimized by using midslice planimetry as opposed to whole kidney measurements and by employing parametric modelling of the kidney using pre-established geometric shapes like ellipsoids or by hybrid level-set methods.[66-71] These approaches for renal segmentation are semi-automated and usually require an expert observer to assist with manually preselecting measurements and/or landmarks in order to initialize the models. Machine learning-based renal segmentation provides a solution for deforming the kidney shape using a constrained statistical model-based algorithm trained upon a dataset.[72] This approach requires minimal user interaction and has made contributions to the field of physiology. Fully automated supervised and unsupervised machine learning algorithms have been explored for renal segmentation using convolutional neuronal network models.[55,72-76]

Recent studies on machine learning-based renal segmentation using neural networks reported processing times as good as 1 to 10 s per subject.[76-78] Although these processing times are superior to our analytic approach, the effort needed to setup meticulously annotated imaging data that can be used to train, validate and test artificial intelligence algorithms must also be included in order to make a fair benchmarking of processing times. Nevertheless, the processing time of the proposed ABSM can be substantially reduced by the application of state-of-the-art global optimization methods like evolutionary algorithms, swarm-based methods, or simulated annealing. Using parallel computing, efficient GPU implementation or high-performance computing hardware provides further means for accelerating the ABSM-based determination of kidney size.

In our preclinical study, the time needed for a given manual segmentation was independent of the prior experience of the observers. Considering the more complex anatomy of the human kidney versus the rat kidney, a thorough manual segmentation of the parenchyma of human kidneys will most likely take more time and require more observer experience than reported here for the rat kidney. Manual planimetry of human kidneys was reported to require segmentation times
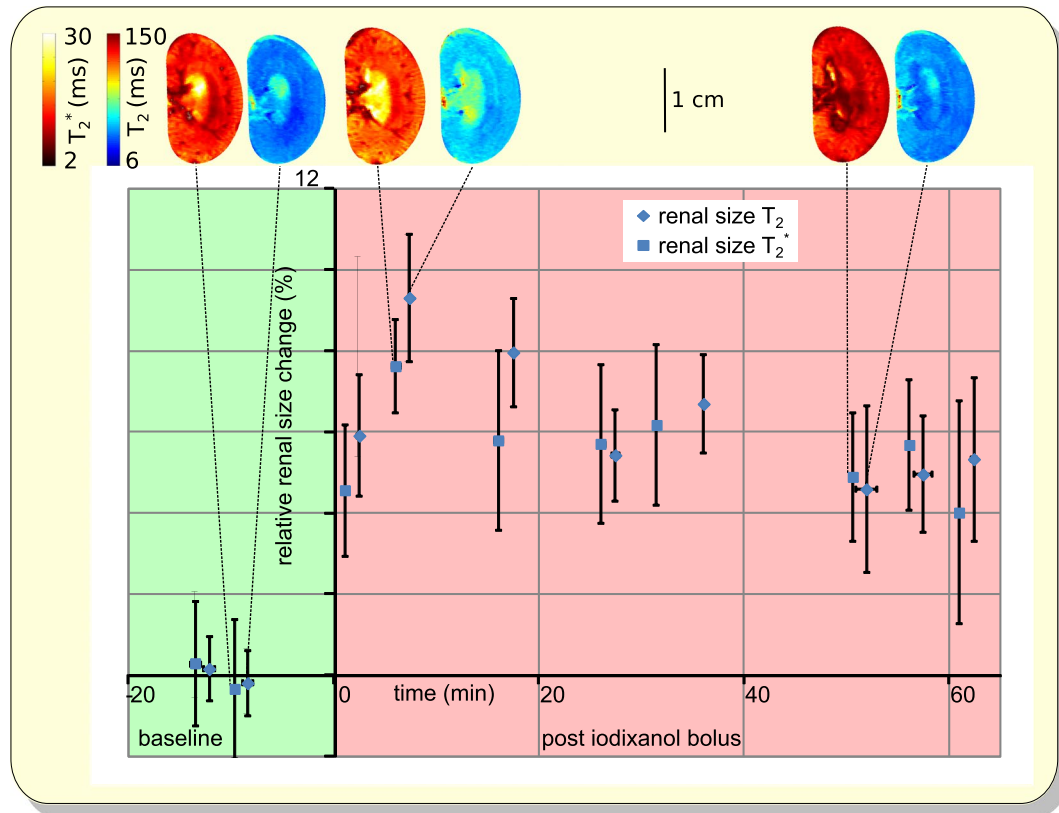
FIGURE 10 Temporal evolution of relative changes in renal size upon bolus administration of the X-ray CM iodixanol derived from T_2 and T_2^* mapping of the kidney using the automatic bean-shaped model. Data obtained for n = 9 rats are given as mean $\pm$ SEM of renal size changes relative to the last T_2 maps obtained before CM injection. Exemplary colour-coded renal T_2^* and T_2 maps (colour scales in milliseconds) are shown above

of 20-45 min on average.[69,71] Thus, automated approaches such as the ABSM as well as machine learning algorithms are urgently needed, along with careful validation under pathophysiological conditions and for a broad range of image contrasts and intensities. These developments will help to promote the potential of MRI in evaluating renal size as a clinical parameter to inform on the various stages of renal pathophysiology and to evaluate treatment of renal disease. To this end, the automated bean-shaped approach has value for MR monitoring of kidney size in translational research and in preclinical models emulating clinical conditions and facilitates systematic analysis of the correlation between renal size and renal oxygenation using T_2 and T_2^* mapping in small rodents in conjunction with simultaneous physiological measurements (MR-PHYSIOL)[52,63,79] by connecting imaging with experimental physiology and data science.[80] MR-based kidney size monitoring during reversible interventions relevant to human beings (eg, changes in the inspiratory gas composition) may also serve to diagnose changes in the viscoelastic properties of the kidney related to disorders such as diffuse renal fibrosis.

To demonstrate the value and relevance of MR-based longitudinal renal size assessment to explore renal pathophysiology, experimental interventions mimicking realistic clinical scenarios were employed to induce alterations in kidney size in rats. For example, several surgical procedures require cross-clamping of the suprarenal aorta or of the renal artery, which if maintained for long periods of time carries the risk of renal ischemia-reperfusion injury.[44,81-83] Renal size monitoring using the ABSM revealed a reduction of ~7% in kidney size during the short-term occlusions of the suprarenal aorta. With the onset of this occlusion, inflow of blood into the kidney is abruptly stopped. At the same time, outflow via the renal vein continues, until pressures in intrarenal vessels and in the vena cava are equalized. This results in a reduction in intrarenal blood volume and manifests itself in the immediate drop in kidney size.[46,52] The restoration of the kidney size upon cessation of the aortic occlusion is rather sluggish, because this occlusion does affect not only the kidneys but also all extrarenal vascular beds downstream of the occluder. During the occlusion, the accumulation of vasodilatory metabolites together with the decrease in tissue pO_2 and pH and the increase in tissue pCO_2 result in vasodilation in this substantial portion of the circulation. Renewed inflow of blood into these vessels upon cessation of the occlusion leads to a marked initial decrease in systemic arterial pressure and, thus, also in renal artery pressure. With the incremental restoration of physiologic conditions in these vascular beds,

arterial pressure is slowly restored, which results in resto-ration of pre-occlusion inflow of blood into the kidney.[46,52]

Renal vein occlusion, which is conducted in clinical pro-cedures such as partial nephrectomy, may also lead to renal ischemia-reperfusion injury.[44,84-86] For occlusion of the left renal vein, renal size tracking with the ABSM detected an in-crease in kidney size of ~5%. With the onset of renal venous occlusion, outflow of blood is abruptly stopped. The inflow of blood via the renal artery does not cease until the arterial pressure-induced distension of intrarenal vessels is counter-balanced by the resistance of the entire renal tissue including the relatively tough renal capsule. This increase in intrarenal blood volume manifests itself in the substantial swelling of the kidney.[46,52,62] Upon cessation of the renal venous occlu-sion, kidney size is restored faster than upon the cessation of the aortic occlusion, because no major effects exerted by vasomotion of extrarenal vascular beds are involved. Thus, kidney size decreases with the outflow of the surplus intrare-nal blood into the vena cava.

Upper urinary tract endourologic procedures often cause temporary increases in tubular as well as intrarenal pressure, with excessive pressures carrying the risks of pyelovenous backflow, damage to tubular integrity and hypoperfusion due to compression of intravascular vessels.[29,87] Renal size track-ing with the ABSM detected an increase in kidney size of ~2% upon elevating the pressure by 30 mm Hg; kidney size returned to baseline shortly after cessation of this pressure elevation.

Intravascular injection of X-ray CM carries the risk of in-ducing AKI, in particular, when large doses are administered intra-arterially (e.g. for cardiac procedures) and a highly vis-cous CM such as iodixanol is used.[34,88,89] The pathophysi-ology is characterized by complex interactions of several mechanisms that result in renal tissue hypoperfusion and hypoxia. One of the major mechanisms is increased fluid vis-cosity that perturbs renal tubulodynamics and haemodynam-ics. In the tubules, X-ray CM become concentrated, as water is reabsorbed, but the CM are not. Consequently, tubular fluid viscosity increases exponentially, which reduces the flow rate and increases intratubular pressure.[34,39,88] Because the renal capsule is relatively rigid, this results in what has been called 'intrarenal compartment syndrome': as intrarenal pressure increases, intrarenal blood vessels become compressed.[31,90] This scenario may explain an apparent discrepancy between earlier findings on renal oxygenation obtained by invasive measurements of tissue pO_2 versus T_2^* mapping with BOLD MRI. Whereas renal tissue pO_2 immediately dropped well below baseline levels upon intra-arterial administration of iodixanol in rats, renal T_2^* transiently increased by up to 20% for about 10 min before it decreased well below control levels.[42,63] As T_2^* reflects the amount of deoxygenated hae-moglobin per tissue volume (voxel), the compression of intra-vascular vessels results in an increase in T_2^* at a time when the blood and tissue oxygenation is deteriorated rather than

improved.[52] Renal size tracking with the ABSM detected a rapid increase in kidney size with peak values of ~9% about 10 min after CM injection, followed by a gradual decrease to ~4% of pre-injection level observed 60 min after CM in-jection. The peak in renal size corresponds with the tran-sient increase in T_2^*. Simultaneous MR-based monitoring of renal size and of renal blood oxygenation level dependent T_2^* may therefore help to correctly interpret changes in renal oxygenation.

Whereas the experimental interventions discussed so far were to be expected—and proved—to result in changes in kidney size, administration of the USPIO preparation feru-moxytol was used as negative control. Intravenous injection of ferumoxytol was previously demonstrated to have no mea-surable effects on control of renal haemodynamics and ox-ygenation and, thereby, on kidney size, whilst substantially altering the MR image contrast due to T_2 and T_2^* shorten-ing.[48,62] Our observation that T_2 and T_2^* shortening due to ferumoxytol does not significantly change the kidney size measured by the ABSM demonstrates that this approach sup-ports renal segmentation for a large dynamic range of MRI signal-to-noise ratios and contrast-to-noise ratios. This dy-namic range exceeds that induced by pathophysiologically relevant interventions or by using other intrinsic MR contrast mechanisms. We confirmed that following administration of ferumoxytol, the ABSM segmentation could detect the same changes in renal size observed upon a second set of reversible interventions compared to the first set of interventions which was performed prior to ferumoxytol injection.

Midslice planimetry is well established in the literature for assessment of renal size. However, it is a relevant caveat that planimetry, including the bean-shaped model, provides only a cross-sectional area rather than renal volume. Therefore, the bean-shaped model, like other single slice assessments, might be less sensitive to alterations in renal size than renal volumetry. Whilst it might be appealing to extend the appli-cation of the ABSM to segment the kidney in 3D data sets, the whole kidney coverage acqusitions come at the cost of increased acquisition time, which is undesireable for patient MRI examinations. Thus, the potential benefit of whole kid-ney volume data versus kidney size assessment based on mid-slice planimetry must be balanced with clinical feasibility. In the preclinical experimental context, the temporal resolution required for longitudinal experiments with physiological interventions such as those used in the current study would be severely constrained by the longer acquisition times that would be needed to obtain 3D data.

In conclusion, our results demonstrate the efficacy of the bean-shaped model to provide automated assessment and quantification of changes in kidney size in small rodents, with accuracy and precision equivalent to that of skilled human observers but requiring substantially less time. This approach supports preclinical studies aimed at elucidating changes in

renal size associated with renal pathology. This approach enables new insights into mechanisms of renal pathophysiology by means of systematic analysis of the relationship between renal size, renal haemodynamics and oxygenation probed with parametric MRI and physiological measurements.

CONFLICT OF INTEREST
The authors declare no conflicts of interest.

DATA AVAILABILITY STATEMENT
The data that support the findings of this study are available from the corresponding author upon reasonable request.

ORCID
Jason M. Millward https://orcid.org/0000-0003-4484-2798
Kathleen Cantow https://orcid.org/0000-0002-3907-6315
Luis Hummel https://orcid.org/0000-0002-6613-6029
Kaixuan Zhao https://orcid.org/0000-0003-4769-7477
João S. Periquito https://orcid.org/0000-0003-3702-9264
Andreas Pohlmann https://orcid.org/0000-0002-8572-2568
Sonia Waiczies https://orcid.org/0000-0002-9916-9572
Erdmann Seeliger https://orcid.org/0000-0002-5685-8044
Thoralf Niendorf https://orcid.org/0000-0001-7584-6527

REFERENCES
1. Luyckx VA, Tonelli M, Stanifer JW. The global burden of kidney disease and the sustainable development goals. *Bull World Health Organ*. 2018;96(6):414-422D.
2. Hoste EAJ, Kellum JA, Selby NM, et al. Global epidemiology and outcomes of acute kidney injury. *Nat Rev Nephrol*. 2018;14(10):607-625.
3. Levin A, Tonelli M, Bonventre J, et al. Global kidney health 2017 and beyond: a roadmap for closing gaps in care, research, and policy. *Lancet*. 2017;390(10105):1888-1917.
4. van Duijl TT, Ruhaak LR, de Fijter JW, Cobbaert CM. Kidney injury biomarkers in an academic hospital setting: where are we now? *Clin Biochem Rev*. 2019;40(2):79-97.
5. Luft FC. Biomarkers and predicting acute kidney injury. *Acta Physiol*. 2020;231:e13479.
6. Schrezenmeier EV, Barasch J, Budde K, Westhoff T, Schmidt-Ott KM. Biomarkers in acute kidney injury—pathophysiological basis and clinical performance. *Acta Physiol*. 2017 ;219(3):554-572.
7. Molitoris BA. Urinary biomarkers: alone are they enough? *J Am Soc Nephrol*. 2015;26(7):1485-1488.
8. Simms R, Sourbron S. Recent findings on the clinical utility of renal magnetic resonance imaging biomarkers. *Nephrol Dial Transplant*. 2020;35(6):915-919.
9. Pickkers P, Ostermann M, Joannidis M, et al. The intensive care medicine agenda on acute kidney injury. *Intensive Care Med*. 2017;43(9):1198-1209.
10. Matejovic M, Ince C, Chawla LS, et al. Renal hemodynamics in AKI. In search of new treatment targets. *J Am Soc Nephrol*. 2016;27(1):49-58.
11. Khwaja A. KDIGO clinical practice guidelines for acute kidney injury. *Nephron Clin Pract*. 2012;120(4):c179-c184.
12. Grenier N, Merville P, Combe C. Radiologic imaging of the renal parenchyma structure and function. *Nat Rev Nephrol*. 2016;12(6):348-359.
13. Zarjou A, Sanders PW, Mehta RL, Agarwal A. Enabling innovative translational research in acute kidney injury. *Clin Transl Sci*. 2012;5(1):93-101.
14. Evans RG, O'Connor PM. Initiation and progression of chronic kidney disease: can we definitively test the chronic hypoxia hypothesis? *Hypertension*. 2013;62(5):827-828.
15. Cantow K, Hummel L, Flemming B, Waiczies S, Niendorf T, Seeliger E. Imagine physiology without imaging. *Acta Physiol*. 2020;230(3):e13549.
16. Niendorf T, Frydman L, Neeman M, Seeliger E. Google maps for tissues: multiscale imaging of biological systems and disease. *Acta Physiol*. 2020;228(2):e13392.
17. Selby NM, Blankestijn PJ, Boor P, et al. Magnetic resonance imaging biomarkers for chronic kidney disease: a position paper from the European Cooperation in Science and Technology Action PARENCHIMA. *Nephrol Dial Transplant*. 2018;33(suppl_2):ii4-ii14.
18. Caroli A, Remuzzi A, Remuzzi G. Does MRI trump pathology? A new era for staging and monitoring of kidney fibrosis. *Kidney Int*. 2020;97(3):442-444.
19. Magistroni R, Corsi C, Marti T, Torra R. A review of the imaging techniques for measuring kidney and cyst volume in establishing autosomal dominant polycystic kidney disease progression. *Am J Nephrol*. 2018;48(1):67-78.
20. Jo WR, Kim SH, Kim KW, et al. Correlations between renal function and the total kidney volume measured on imaging for autosomal dominant polycystic kidney disease: a systematic review and meta-analysis. *Eur J Radiol*. 2017;95:56-65.
21. Grantham JJ, Torres VE. The importance of total kidney volume in evaluating progression of polycystic kidney disease. *Nat Rev Nephrol*. 2016;12(11):667-677.
22. Administration USFaD. Qualification of biomarker total kidney volume in studies for treatment of autosomal dominant polycystic kidney disease 2015. Accessed November 10, 2020.
23. Agency EM. Qualification opinion - Total Kidney Volume (TKV) as a prognostic biomarker for use in clinical trials evaluating patients with Autosomal Dominant Polycystic Kidney Disease (ADPKD). *Qualification Opinion* [pdf document]. 2015. Accessed November 10, 2020.
24. Buturovic-Ponikvar J, Visnar-Perovic A. Ultrasonography in chronic renal failure. *Eur J Radiol*. 2003;46(2):115-122.

25. Buchanan CE, Mahmoud H, Cox EF, et al. Quantitative assessment of renal structural and functional changes in chronic kidney disease using multi-parametric magnetic resonance imaging. *Nephrol Dial Transplant*. 2020;35(6):955-964.

26. Gooding KM, Lienczewski C, Papale M, et al. Prognostic imaging biomarkers for diabetic kidney disease (iBEAt): study protocol. *BMC Nephrol*. 2020;21(1):242.

27. Gottschalk CW, Mylle M. Micropuncture study of pressures in proximal tubules and peritubular capillaries of the rat kidney and their relation to ureteral and renal venous pressures. *Am J Physiol*. 1956;185(2):430-439.

28. Gottschalk CW, Mylle M. Micropuncture study of pressures in proximal and distal tubules and peritubular capillaries of the rat kidney during osmotic diuresis. *Am J Physiol*. 1957;189(2):323-328.

29. Tokas T, Herrmann TRW, Skolarikos A, Nagele U. Pressure matters: intrarenal pressures during normal and pathological conditions, and impact of increased values to renal physiology. *World J Urol*. 2019;37(1):125-131.

30. Wen JG, Ringgaard S, Jorgensen TM, Stodkilde-Jorgensen H, Djurhuus JC, Frokiaer J. Long-term effects of partial unilateral ureteral obstruction on renal hemodynamics and morphology in newborn rats: a magnetic resonance imaging study. *Urol Res*. 2002;30(4):205-212.

31. Evans RG. Renal decapsulation to treat ischemic acute kidney injury: a new twist in an old tale. *Crit Care Med*. 2018;46(2):332-333.

32. Zuk A, Bonventre JV. Recent advances in acute kidney injury and its consequences and impact on chronic kidney disease. *Curr Opin Nephrol Hypertens*. 2019;28(4):397-405.

33. Brezis M, Rosen S. Hypoxia of the renal medulla–its implications for disease. *N Engl J Med*. 1995;332:647-655.

34. Fähling M, Seeliger E, Patzak A, Persson PB. Understanding and preventing contrast-induced acute kidney injury. *Nat Rev Nephrol*. 2017;13(3):169-180.

35. Evans RG, Ince C, Joles JA, et al. Haemodynamic influences on kidney oxygenation: clinical implications of integrative physiology. *Clin Exp Pharmacol Physiol*. 2013;40(2):106-122.

36. Evans RG, Ow CP, Bie P. The chronic hypoxia hypothesis: the search for the smoking gun goes on. *Am J Physiol Renal Physiol*. 2015;308(2):F101-F102.

37. Calzavacca P, Evans RG, Bailey M, Bellomo R, May CN. Cortical and medullary tissue perfusion and oxygenation in experimental septic acute kidney injury. *Crit Care Med*. 2015;43(10):e431-e439.

38. Ma S, Evans RG, Iguchi N, et al. Sepsis-induced acute kidney injury: a disease of the microcirculation. *Microcirculation*. 2019;26(2):e12483.

39. Seeliger E, Sendeski M, Rihal CS, Persson PB. Contrast-induced kidney injury: mechanisms, risk factors, and prevention. *Eur Heart J*. 2012;33(16):2007-2015.

40. Ueda J, Nygren A, Hansell P, Ulfendahl HR. Effect of intravenous contrast media on proximal and distal tubular hydrostatic pressure in the rat kidney. *Acta Radiol*. 1993;34(1):83-87.

41. Seeliger E, Becker K, Ladwig M, Wronski T, Persson PB, Flemming B. Up to 50-fold increase in urine viscosity with iso-osmolar contrast media in the rat. *Radiology*. 2010;256(2):406-414.

42. Seeliger E, Cantow K, Arakelyan K, Ladwig M, Persson PB, Flemming B. Low-dose nitrite alleviates early effects of an X-ray contrast medium on renal hemodynamics and oxygenation in rats. *Invest Radiol*. 2014;49(2):70-77.

43. Seeliger E, Lenhard DC, Persson PB. Contrast media viscosity versus osmolality in kidney injury: lessons from animal studies. *Biomed Res Int*. 2014;2014:358136.

44. Cao J, Zhu S, Ye M, et al. Comparison of renal artery vs renal artery-vein clamping during partial nephrectomy: a system review and meta-analysis. *J Endourol*. 2020;34(4):523-530.

45. Adams LC, Ralla B, Bender Y-N, et al. Renal cell carcinoma with venous extension: prediction of inferior vena cava wall invasion by MRI. *Cancer Imaging*. 2018;18(1):17.

46. Grosenick D, Cantow K, Arakelyan K, et al. Detailing renal hemodynamics and oxygenation in rats by a combined near-infrared spectroscopy and invasive probe approach. *Biomed Opt Express*. 2015;6(2):309-323.

47. Haase M, Bellomo R, Story D, et al. Effect of mean arterial pressure, haemoglobin and blood transfusion during cardiopulmonary bypass on post-operative acute kidney injury. *Nephrol Dial Transplant*. 2012;27(1):153-160.

48. Cantow K, Pohlmann A, Flemming B, et al. Acute effects of ferumoxytol on regulation of renal hemodynamics and oxygenation. *Sci Rep*. 2016;20(6):29965. https://doi.org/10.1038/srep29965.

49. Evans RG, Smith DW, Lee CJ, Ngo JP, Gardiner BS. What Makes the kidney susceptible to hypoxia? *Anat Rec*. 2020;303(10):2544-2552.

50. Joles JA. Tailoring cardiopulmonary bypass pump flow and mean arterial pressure to maintain renal oxygenation. *Acta Physiol*. 2021;231(4):e13619.

51. Evans RG, Iguchi N, Cochrane AD, et al. Renal hemodynamics and oxygenation during experimental cardiopulmonary bypass in sheep under total intravenous anesthesia. *Am J Physiol Regul Integr Comp Physiol*. 2020;318(2):R206-R213.

52. Pohlmann A, Arakelyan K, Hentschel J, et al. Detailing the relation between renal T2* and renal tissue pO2 using an integrated approach of parametric magnetic resonance imaging and invasive physiological measurements. *Invest Radiol*. 2014;49(8):547-560.

53. Pohlmann A, Cantow K, Hentschel J, et al. Linking non-invasive parametric MRI with invasive physiological measurements (MR-PHYSIOL): towards a hybrid and integrated approach for investigation of acute kidney injury in rats. *Acta Physiol*. 2013;207(4):673-689.

54. Bak M, Thomsen K, Christiansen T, Flyvbjerg A. Renal enlargement precedes renal hyperfiltration in early experimental diabetes in rats. *J Am Soc Nephrol*. 2000;11(7):1287-1292.

55. Edwards ME, Periyanan S, Anaam D, Gregory AV, Kline TL. Automated total kidney volume measurements in pre-clinical magnetic resonance imaging for resourcing imaging data, annotations, and source code. *Kidney Int*. 2021;99(3):763–766. https://doi.org/10.1016/j.kint.2020.07.040.

56. Erokwu BO, Anderson CE, Flask CA, Dell KM. Quantitative magnetic resonance imaging assessments of autosomal recessive polycystic kidney disease progression and response to therapy in an animal model. *Pediatr Res*. 2018;83(5):1067-1074.

57. Hueper K, Hensen B, Gutberlet M, et al. Kidney transplantation: multiparametric functional magnetic resonance imaging for assessment of renal allograft pathophysiology in mice. *Invest Radiol*. 2016;51(1):58-65.

58. Xie L, Cianciolo RE, Hulette B, et al. Magnetic resonance histology of age-related nephropathy in the Sprague Dawley rat. *Toxicol Pathol*. 2012;40(5):764-778.

59. Jiang K, Tang H, Mishra PK, Macura SI, Lerman LO. Measurement of murine kidney functional biomarkers using DCE-MRI: a multi-slice TRICKS technique and semi-automated image processing algorithm. *Magn Reson Imaging*. 2019;63:226-234.

60. Cantow K, Evans RG, Grosenick D, et al. Quantitative assessment of renal perfusion and oxygenation by invasive probes: basic concepts. *Methods Mol Biol*. 2021;2216:89-107.

61. Cantow K, Ladwig-Wiegard M, Flemming B, Pohlmann A, Niendorf T, Seeliger E. Monitoring renal hemodynamics and oxygenation by invasive probes: experimental protocol. *Methods Mol Biol*. 2021;2216:327-347.

62. Pohlmann A, Cantow K, Huelnhagen T, et al. Experimental MRI monitoring of renal blood volume fraction variations En route to renal magnetic resonance oximetry. *Tomography*. 2017;3(4):188-200.

63. Arakelyan K, Cantow K, Hentschel J, et al. Early effects of an x-ray contrast medium on renal T(2) */T(2) MRI as compared to short-term hyperoxia, hypoxia and aortic occlusion in rats. *Acta Physiol*. 2013;208(2):202-213.

64. Yushkevich PA, Piven J, Hazlett HC, et al. User-guided 3D active contour segmentation of anatomical structures: significantly improved efficiency and reliability. *NeuroImage*. 2006;31(3):1116-1128.

65. Hosszu A, Kaucsar T, Seeliger E, Fekete A. Animal models of renal pathophysiology and disease. *Methods Mol Biol*. 2021;2216:27-44.

66. Seuss H, Janka R, Prümmer M, et al. Development and evaluation of a semi-automated segmentation tool and a modified ellipsoid formula for volumetric analysis of the kidney in non-contrast T2-weighted MR images. *J Digit Imaging*. 2017;30(2):244-254.

67. Bakker J, Olree M, Kaatee R, et al. Renal volume measurements: accuracy and repeatability of US compared with that of MR imaging. *Radiology*. 1999;211(3):623-628.

68. Irazabal MV, Rangel LJ, Bergstralh EJ, et al. Imaging classification of autosomal dominant polycystic kidney disease: a simple model for selecting patients for clinical trials. *J Am Soc Nephrol*. 2015;26(1):160-172.

69. Sharma K, Caroli A, Quach LV, et al. Kidney volume measurement methods for clinical studies on autosomal dominant polycystic kidney disease. *PLOS ONE*. 2017;12(5):e0178488.

70. Bae KT, Tao C, Wang J, et al. Novel approach to estimate kidney and cyst volumes using mid-slice magnetic resonance images in polycystic kidney disease. *Am J Nephrol*. 2013;38(4):333-341.

71. Simms RJ, Doshi T, Metherall P, et al. A rapid high-performance semi-automated tool to measure total kidney volume from MRI in autosomal dominant polycystic kidney disease. *Eur Radiol*. 2019;29(8):4188-4197.

72. Gloger O, Tonnies K, Laqua R, Volzke H. Fully automated renal tissue volumetry in MR volume data using prior-shape-based segmentation in subject-specific probability maps. *IEEE Trans Biomed Eng*. 2015;62(10):2338-2351.

73. van Gastel MDA, Edwards ME, Torres VE, Erickson BJ, Gansevoort RT, Kline TL. Automatic measurement of kidney and liver volumes from MR images of patients affected by autosomal dominant polycystic kidney disease. *J Am Soc Nephrol*. 2019;30(8):1514-1522.

74. Gloger O, Tonnies K, Mensel B, Volzke H. Fully automatized renal parenchyma volumetry using a support vector machine based recognition system for subject-specific probability map generation in native MR volume data. *Phys Med Biol*. 2015;60(22):8675-8693.

75. Kline TL, Korfiatis P, Edwards ME, et al. Performance of an artificial multi-observer deep neural network for fully automated segmentation of polycystic kidneys. *J Digit Imaging*. 2017;30(4):442-448.

76. Sharma K, Rupprecht C, Caroli A, et al. Automatic segmentation of kidneys using deep learning for total kidney volume quantification in autosomal dominant polycystic kidney disease. *Sci Rep*. 2017;7(1):2049.

77. Langner T, Östling A, Maldonis L, et al. Kidney segmentation in neck-to-knee body MRI of 40,000 UK Biobank participants. *Sci Rep*. 2020;10(1):20963.

78. Daniel AJ, Buchanan CE, Allcock T, et al. Automated renal segmentation in healthy and chronic kidney disease subjects using a convolutional neural network. *Magn Reson Med*. 2021;86(2):1125-1136.

79. Niendorf T, Pohlmann A, Arakelyan K, et al. How bold is blood oxygenation level-dependent (BOLD) magnetic resonance imaging of the kidney? Opportunities, challenges and future directions. *Acta Physiol*. 2015;213(1):19-38.

80. Gardiner BS, Smith DW, Lee CJ, Ngo JP, Evans RG. Renal oxygenation: from data to insight. *Acta Physiol*. 2020;228(4):e13450.

81. Martelli E, Cho JS. Merits of and technical tips for supra-mesenteric aortic cross clamping. *Vasc Specialist Int*. 2019;35(2):55-59.

82. Ballard JL. Thoracoabdominal aortic aneurysm repair: historical review and description of a re-engineered technique. *Perspect Vasc Surg Endovasc Ther*. 2005;17(3):207-215.

83. Jongkind V, Yeung KK, Akkersdijk GJM, et al. Juxtarenal aortic aneurysm repair. *J Vasc Surg*. 2010;52(3):760-767.

84. Cozar JM, Tallada M. Open partial nephrectomy in renal cancer: a feasible gold standard technique in all hospitals. *Adv Urol*. 2008:2008:916463.

85. Park Y, Hirose R, Dang K, et al. Increased severity of renal ischemia-reperfusion injury with venous clamping compared to arterial clamping in a rat model. *Surgery*. 2008;143(2):243-251.

86. Li X, Liu M, Bedja D, et al. Acute renal venous obstruction is more detrimental to the kidney than arterial occlusion: implication for murine models of acute kidney injury. *Am J Physiol Renal Physiol*. 2012;302(5):F519-F525.

87. Tokas T, Skolarikos A, Herrmann TRW, Nagele U. Pressure matters 2: intrarenal pressure ranges during upper-tract endourological procedures. *World J Urol*. 2019;37(1):133-142.

88. Seeliger E, Persson PB. Kidney damage by iodinated contrast media. *Acta Physiol*. 2019;227(4):e13259.

89. Liu ZZ, Schmerbach K, Lu Y, et al. Iodinated contrast media cause direct tubular cell damage, leading to oxidative stress, low nitric oxide, and impairment of tubuloglomerular feedback. *Am J Physiol Renal Physiol*. 2014;306(8):F864-872.

90. Cruces P, Lillo P, Salas C, et al. Renal decapsulation prevents intrinsic renal compartment syndrome in ischemia-reperfusion-induced acute kidney injury: a physiologic approach. *Crit Care Med*. 2018;46(2):216-222.